NASA/TM—2003-212731

Computations of Internal and External Axisymmetric Nozzle Aerodynamics at Transonic Speeds

Teryn DalBello
University of Toledo, Toledo, Ohio

Nicholas Georgiadis and Dennis Yoder
Glenn Research Center, Cleveland, Ohio

Theo Keith
University of Toledo, Toledo, Ohio

November 2003

The NASA STI Program Office . . . in Profile

Since its founding, NASA has been dedicated to the advancement of aeronautics and space science. The NASA Scientific and Technical Information (STI) Program Office plays a key part in helping NASA maintain this important role.

The NASA STI Program Office is operated by Langley Research Center, the Lead Center for NASA's scientific and technical information. The NASA STI Program Office provides access to the NASA STI Database, the largest collection of aeronautical and space science STI in the world. The Program Office is also NASA's institutional mechanism for disseminating the results of its research and development activities. These results are published by NASA in the NASA STI Report Series, which includes the following report types:

- TECHNICAL PUBLICATION. Reports of completed research or a major significant phase of research that present the results of NASA programs and include extensive data or theoretical analysis. Includes compilations of significant scientific and technical data and information deemed to be of continuing reference value. NASA's counterpart of peer-reviewed formal professional papers but has less stringent limitations on manuscript length and extent of graphic presentations.

- TECHNICAL MEMORANDUM. Scientific and technical findings that are preliminary or of specialized interest, e.g., quick release reports, working papers, and bibliographies that contain minimal annotation. Does not contain extensive analysis.

- CONTRACTOR REPORT. Scientific and technical findings by NASA-sponsored contractors and grantees.

- CONFERENCE PUBLICATION. Collected papers from scientific and technical conferences, symposia, seminars, or other meetings sponsored or cosponsored by NASA.

- SPECIAL PUBLICATION. Scientific, technical, or historical information from NASA programs, projects, and missions, often concerned with subjects having substantial public interest.

- TECHNICAL TRANSLATION. English-language translations of foreign scientific and technical material pertinent to NASA's mission.

Specialized services that complement the STI Program Office's diverse offerings include creating custom thesauri, building customized databases, organizing and publishing research results . . . even providing videos.

For more information about the NASA STI Program Office, see the following:

- Access the NASA STI Program Home Page at ***http://www.sti.nasa.gov***

- E-mail your question via the Internet to help@sti.nasa.gov

- Fax your question to the NASA Access Help Desk at 301–621–0134

- Telephone the NASA Access Help Desk at 301–621–0390

- Write to:
  NASA Access Help Desk
  NASA Center for AeroSpace Information
  7121 Standard Drive
  Hanover, MD 21076

NASA/TM—2003-212731

Computations of Internal and External Axisymmetric Nozzle Aerodynamics at Transonic Speeds

Teryn DalBello
University of Toledo, Toledo, Ohio

Nicholas Georgiadis and Dennis Yoder
Glenn Research Center, Cleveland, Ohio

Theo Keith
University of Toledo, Toledo, Ohio

Prepared for the
39th Combustion/27th Airbreathing Propulsion/21st Propulsion Systems Hazards/
Third Modeling and Simulation Joint Subcommittee Meeting
sponsored by the Joint-Army-Navy-Air Force Interagency Propulsion Committee (JANNAF)
Colorado Springs, Colorado, December 1–5, 2003

National Aeronautics and
Space Administration

Glenn Research Center

November 2003

This work was sponsored by the Low Emissions Alternative Power Project of the Vehicle Systems Program at the NASA Glenn Research Center.

Available from

NASA Center for Aerospace Information
7121 Standard Drive
Hanover, MD 21076

National Technical Information Service
5285 Port Royal Road
Springfield, VA 22100

Available electronically at http://gltrs.grc.nasa.gov

Computations of Internal and External Axisymmetric Nozzle Aerodynamics at Transonic Speeds

Teryn DalBello
University of Toledo
Toledo, Ohio 43606

Nicholas Georgiadis and Dennis Yoder
National Aeronautics and Space Administration
Glenn Research Center
Cleveland, Ohio 44135

Theo Keith
University of Toledo
Toledo, Ohio 43606

ABSTRACT

Computational Fluid Dynamics (CFD) analyses of axisymmetric circular-arc boattail nozzles have been completed in support of NASA's Next Generation Launch Technology Program to investigate the effects of high-speed nozzle geometries on the nozzle internal flow and the surrounding boattail regions. These computations span the very difficult transonic flight regime, with shock-induced separations and strong adverse pressure gradients. External afterbody and internal nozzle pressure distributions computed with the Wind code are compared with experimental data. A range of turbulence models were examined in Wind, including an Explicit Algebraic Stress model (EASM). Computations on two nozzle geometries have been completed at freestream Mach numbers ranging from 0.6 to 0.9, driven by nozzle pressure ratios (NPR) ranging from 2.9 to 5. Results obtained on converging-only geometry indicate reasonable agreement to experimental data, with the EASM and Shear Stress Transport (SST) turbulence models providing the best agreement. Calculations completed on a converging-diverging geometry involving large-scale internal flow separation did not converge to a true steady-state solution when run with variable timestepping (steady-state). Calculations obtained using constant timestepping (time-accurate) indicate less variations in flow properties compared with steady-state solutions. This failure to converge to a steady-state solution was found to be the result of difficulties in using variable time-stepping with large-scale separations present in the flow. Nevertheless, time-averaged boattail surface pressure coefficient and internal nozzle pressures show fairly good agreement with experimental data. The SST turbulence model demonstrates the best overall agreement with experimental data.

INTRODUCTION

Computational Fluid Dynamics (CFD) analyses of an axisymmetric nozzles at transonic freestream conditions have been completed to determine the capabilities of Reynolds-Averaged Navier-Stokes (RANS) calculations to predict the details of off-design nozzle performance. The purpose of this study is to gain an understanding of the flow field surrounding boattail-nozzle configurations at transonic speeds, including the effects of jet exhaust on the flowfield, and to compare computed values to experimental data in support of future high-speed nozzle studies for NASA's Next Generation Launch Technology Program. External and internal nozzle pressure distributions computed with the Wind code are compared with experimental data obtained in the NASA Langley 16-Foot Transonic Tunnel.[1]

At transonic freestream Mach numbers, poor nozzle performance can significantly affect overall propulsion system performance. In particular, high nozzle afterbody (boattail) drag, consisting of a combination of pressure drag (separated flow), viscous drag (skin friction), and wave drag is a primary source of poor nozzle performance. The nozzle pressure ratio and nozzle geometry determine the pressure differences that result between the jet and freestream flows, which, in turn, governs the amount of drag associated with the propulsion system (including the afterbody or boattail surface). Even under the best of conditions with on-design nozzle operation, nozzle afterbody drag usually manifests itself as pressure drag and wave drag. The off-design operation of the nozzles studied in this paper provides an even more challenging environment to test computational tools due to shock-induced separations and strong adverse pressure gradients present.

In this study, computations on two nozzle geometries have been completed at different freestream Mach numbers and nozzle pressure ratios (NPR). The first geometry, referred to as the "Configuration 1" geometry of Abeyounis and Putnam[2], is a converging nozzle (Figure 1) operating at freestream numbers of Mach 0.6 and 0.8 at an NPR of 2.9, and Mach 0.8 at an NPR of 5. This is referred to as Case 1 in this paper. Abeyounis and Putnam conducted investigations to determine the effects of jet exhaust on the subsonic flow surrounding two converging boattail nozzles with attached and separated boundary layers.

The second geometry, from Carson and Lee[3], is a converging-diverging nozzle (Figure 2) operating at freestream Mach numbers of 0.9 and 1.2 at an NPR of 4. This is referred to as Case 2 in this paper. Carson and Lee investigated the internal and external pressure distributions on a wide range of converging-diverging nozzles at various Mach numbers and pressure ratios using an interchangeable mechanism on the test rig installed in the Langley 16-Foot Transonic Tunnel. The nozzles were installed on the aft end of a generic axisymmetric forebody consisting of a conical nose followed by a straight initial afterbody section.

The rig used to obtain experimental results for both cases is shown in Figure 3. Calculated surface pressures, internal and external to the nozzle, for these two cases are compared to experimental data.

NUMERICAL MODEL

Calculations were conducted with Wind[4], a general purpose 3-D Computational Fluid Dynamics code which solves the turbulent, time-dependent, RANS equations using a node-centered finite volume approach. Wind is the production solver of the NPARC Alliance, a joint code development group of NASA Glenn Research Center, USAF Arnold Engineering Development Center, and the Boeing Company. Wind version 5 was used for the steady-state calculations and a test version of Wind with improved second-order time-stepping was used for the time-accurate calculations. The solver was configured to run with the following specifications:

- Axisymmetric flow
- Constant timestepping (time-accurate) and variable timestepping (steady-state)
- Second-order Roe upwind scheme with modification for stretched grids, and second-order time-marching
- One-equation Spalart-Allmaras[5] (S-A), Two-equation Menter Shear Stress Transport[6] (SST), Chien k-ε[7], and Rumsey-Gatski[8,9] k-ε Explicit Algebraic Reynolds Stress (EASM) turbulence models
- Perfect gas, air, γ=1.4

The Spalart-Allmaras turbulence model works well for attached and separated wall bounded flows such as the flow around airfoils. The Chien k-ε model was developed to handle shear layer flows and jet flows. The SST model combines the k-ω formulation to treat inner regions of wall boundary layers with a transformed k-ε formulation to handle the outer, mixing regions of the flow. The EASM model has been recently installed in Wind to better predict compressible jet flows.

The various turbulence models in Wind employ corrections to make them more broadly adaptable to various geometries and conditions. The k-ε model has two corrections, namely the Sarkar Compressibility Correction[10] and the Variable C_μ correction[11]. The Sarkar approximation, which is designed to improve the prediction of compressible jet flows, is used for all computations shown in this paper. However, results for the variable C_μ option are completed both ON and OFF. When activated, this option reduces turbulent viscosity in regions where the production of turbulent kinetic energy is significantly larger than the rate of dissipation. The S-A model was run with and without the streamwise curvature/rotation correction (cc).

The inflow conditions were specified using the *Freestream* and *Arbitrary Inflow* boundary conditions. The *Freestream* BC is used external to the nozzle and the *Arbitrary Inflow* is used at the nozzle inflow plane. Total pressure and total temperature were specified and held constant at the inflow boundaries. The static pressure at the outflow boundary was specified to the value of the freestream pressure in subsonic conditions, and supersonic points were extrapolated. The no-slip condition is used on the nozzle internal and external surfaces.

Wind was configured to run in multi-processor mode on an SGI Origin 2000. Solutions for Case 1 took approximately 12 hours total CPU time. Case 2 steady-state solutions took approximately 20 hours of total CPU time at CFL numbers between 0.6 and 0.8. Case 2 time-accurate solutions took approximately 296 total CPU hours at a timestep of 1 nanosecond.

The convergence criterion consisted of monitoring nozzle thrust for changes with iteration, adequate reduction of the overall solution residual, and mass flow conservation within the nozzle.

COMPUTATIONAL GRIDS AND GEOMETRY DEFINITION

Axisymmetric, structured, computational grids were generated for all cases using Pointwise, Inc's GRIDGEN[12] version 14 software. In all cases, the nozzle is attached to a forebody, whose geometry is included in the computational model due to the well-developed boundary layers along the length of the body.

The computational grid for Case 1 can be seen in Figures 4(a), 4(b), and 4(c). This grid has 33,815 total points spread over 6 zones. The length of the entire assembly L is 149 cm (58.7 inches). The downward curvature of the boattail occurs approximately at an x/L of -0.03. The upstream nozzle diameter is 15.24 cm and acts as the normalizing length. The downstream nozzle diameter is 7.62 cm. The forebody tip is located at station x=-141.38 cm and the boattail nozzle exit is located at station x=+7.62 cm. The computational domain extends to about 7 nozzle diameters vertically, and extends downstream about 50 nozzle diameters. A grid dependence study was conducted on three different grid levels, the coarse being a total of 33,815 points. The medium grid contained 30% more grid points, and the fine grid contained 60% more grid points than the coarse grid. Plots of the mean values of Cp over the boattail surface (Figure 5) indicate that the coarse grid is sufficient to capture the pressure distributions, and, as a result, the coarse grid was used to obtain the results shown in this paper.

The grid for Case 2 can be seen in Figures 6(a), 6(b), and 6(c). This grid has 60,400 total points spread over 5 zones. The computational domain extends radially to about 19 nozzle diameters and extends downstream about 50 nozzle diameters. The maximum nozzle outside diameter D is 15.24 cm and acts as the normalizing length. The entire assembly is about 157 cm (62 inches) long. The downward curvature of the boattail occurs approximately at an x/D of 0. The forebody tip is located at station x=-141.38 cm and the boattail nozzle exit is located at station x=+15.24 cm. A grid dependence study has been conducted on three different grid levels, the coarse being a total of 60,400 points. The medium grid contained 30% more grid points, and the fine grid contained 60% more grid points than the coarse grid. Plots of Cp values over the boattail surface (Figure 7) indicate that the coarse grid is sufficient to capture the pressure distributions. As a result, the coarse grid was used to obtain the results shown in this paper.

Due to the axisymmetric nature of the problems examined here, images presented in this report are mirrored about the symmetry axis in the figures for clarity. Zonal boundaries were organized in such a way that very complex regions of the flow (such as shear layers) do not run parallel to the zonal boundaries. Average y+ values on the viscous walls were specified to be approximately 1.

DESCRIPTION OF CASES AND RESULTS

Results are presented as pressure distributions on the internal and external nozzle surfaces and Mach number contours of the flowfield. Pressure is the primary quantity compared to experimental data because of the direct relation between pressure and the aerodynamic drag associated with the given nozzle shape.

In order to provide a direct comparison with experimental data, results are represented by pressure coefficient curves on the upper boattail surface, and curves of p/p_t (static pressure divided by the nozzle total pressure) on the internal surface. The pressure coefficient Cp used in this analysis is defined as the local pressure minus the freestream pressure divided by the freestream dynamic pressure. For Case 1, the steady-

state pressures are plotted. For Case 2, the plotted pressures are averages of the instantaneous values across 15,000 to 25,000 thousand iterations. In addition, gross thrust is normalized by ideal thrust, and mass flow normalized by ideal mass flow. During the course of the computations, variations in the flow properties were seen in the steady-state calculations requiring subsequent analysis using time-accurate calculations to determine the significance of the variations.

Case #1: Nozzle of Abeyounis and Putnam

Case 1 represents a circular arc convergent nozzle. The relatively steep downward slope of the boattail surface (34 degrees at the trailing edge) results in an adverse pressure gradient and separation on the top surface. The flow conditions are shown in Table 1. Due to the favorable pressure gradient inside the nozzle, there is no separation on the internal surface. The different subcases, constituting the different conditions that were run, are discussed next.

Table 1: Case 1 Flow Conditions

	Subcase 1A	Subcase 1B	Subcase 1C
Freestream Mach Number	0.8	0.8	0.6
Nozzle Total Temperature	534.6 R (297 K)	534.6 R (297 K)	534.6 R (297 K)
Nozzle Total Pressure	27.94 psi (193 kPa)	48.18 psi (332 kPa)	33.42 psi (230 kPa)
Freestream Static Pressure	9.64 psi (66.5 kPa)	9.64 psi (66.5 kPa)	11.53 psi (79.5 kPa)

Subcase 1A: Mach 0.8, NPR 2.9

Figures 8(a) and 8(b) show the Mach number contours for the solution run with the Spalart-Allmaras turbulence model. A series of shock/expansion waves are present in the jet plume, driven by the underexpanded flow exiting the nozzle. Starting at about 0.025 x/L as illustrated in Figure 9, separated flow can be seen on the external surface towards the most rearward points of the boattail. The S-A model predicts the smallest separation bubble and EASM the largest.

The results for each of the turbulence models had very similar qualitative features when examining Mach number contours, for example; results are better seen by examining them quantitatively. Cp is plotted across the boattail surface as shown in Figure 10. The minimum point in Cp occurs at about x/L of -0.015, the point of maximum flow acceleration. The S-A and k-ε models provide the best prediction of the minimum Cp, while the EASM and SST models predict the experimental data the best for x/L greater than 0 (towards the rearward parts of the boattail and in the separation region). Again, the curvature/rotation correction for the S-A model offers a significant improvement over the standard S-A model in the separated region. The k-ε and standard S-A models without the curvature correction showed the most deviation from experiment near the nozzle exit.

Subcase 1B: Mach 0.8, NPR 5

Figure 11 shows the Mach number contours with the S-A model. The sonic, underexpanded flow expands beyond the confines (edges) of the nozzle exit. Expansion waves emanating off the nozzle trailing edge coalesce downstream to form a cone-shaped structure where the maximum Mach number is approximately 2.7.

Figure 12 shows the Cp values on the upper surface for Subcase 1B. It can be seen that all models agree fairly well up to where separation starts to occur (flattening of the Cp curve), or about 0.02 x/L. The EASM model overpredicts the pressure prior to separation (from an x/L of -0.03 to 0.018). The EASM and SST models are closest to experimental data across the entire boattail overall. The SST slightly overpredicts the pressure distribution near the nozzle exit (analogous to Figure 10), with EASM very close to experimental results in the separated region. The curvature/rotation correction for the S-A model offers a significant improvement over the standard S-A model with no corrections. The k-ε and standard S-A without the curvature correction showed the most deviation from experiment near the nozzle exit.

Subcase 1C: Mach 0.6, NPR 2.9

Figure 13 shows the Mach number contours with the S-A model. Expansion waves emanate from the nozzle exit edges and form a cone-like region of Mach number 1.65, similar in structure to Subcase 1B, but with not quite as dramatic a flow expansion. The pressure increase that the jet flow experiences as it exits the nozzle is the difference in magnitude between the jet flow and external flow. Hence, the strength of the shocks (as depicted by the Mach number contours) for this subcase is somewhere between Subcases 1A and 1B. Examining the Cp curves in Figure 14 reveals that the EASM model provides the best overall comparison to experimental data, with better agreement from x/L of -0.03 to 0.018 compared with Subcase 1B. The EASM results slightly overpredict pressures elsewhere on the boattail, while the SST model predicts about the same values for Cp as in Subcase 1A near the nozzle exit. Again, the curvature/rotation correction of the S-A model predicts the pressure distribution more accurately than the standard S-A model. Overall, the EASM and SST models appear to predict the pressure distribution the best. A comparison of Figures 12 and 14 versus Figure 10 reveals that having a larger pressure difference between the jet and the external flow (at the nozzle exit) allows the EASM to better predict the experimental data.

Case #2: Nozzle of Carson and Lee

The results for the convergent-divergent nozzle of Carson and Lee, referred to as the "Configuration 2" nozzle, are presented next. Designed to operate at an NPR of 21.23, this nozzle was run at an off-design at freestream Mach numbers 0.9 and 1.2 and an NPR of 4, resulting in overexpanded flow. The relatively shallow downward slope (3.817 degrees) of the external surface results in attached flow across the entire upper surface. The inner nozzle is cone-shaped (straight wall contour) with a half angle of 13.18 degrees. This results in separation on the inner surface for all NPRs below 6.

Generally, all solutions showed flow accelerating supersonically through the nozzle, followed by the formation of a sophisticated array of shocks and expansion waves. This complex set of expansion and shock waves resulted in apparent unsteadiness near the nozzle exit, affecting the pressure distribution on the top surface. The pressure values for both the steady-state and time-accurate solutions on the internal and external surfaces were time- or iteration-averaged across several thousand iterations to obtain the mean values. These values are compared to experimental data. As a reference, the on-design solution (NPR=21.23) for the "Configuration 2" nozzle is shown in Figure 15. Note that even for this case, the divergent section of the nozzle is not optimized to provide an isentropic expansion of the flow.

The two subcases are examined in more detail below. In addition to the steady-state calculations using all turbulence models common to the two subcases, the unsteady nature of Subcase 2A resulted in additional time-accurate calculation using the SST model. The flow conditions are shown in Table 2.

Table 2: Nozzle flow conditions

	Subcase 2A	Subcase 2B
Freestream Mach Number	0.9	1.2
Nozzle Total Temperature	540.0 R (300 K)	540.0 R (300 K)
Nozzle Total Pressure	34.8 psi (240 kPa)	24.3 psi (168 kPa)
Freestream Static Pressure	8.69 psi (59.9 kPa)	6.06 psi (41.8 kPa)

Subcase 2A: Mach 0.9, NPR 4

First the steady-state solutions will be discussed, followed by discussion of a time-accurate computation using the SST turbulence model.

STEADY-STATE CALCULATIONS

Figure 16(a) shows a qualitative view of Mach number contours using the S-A model, and Figure 16(b) shows contours in detail near the nozzle exit. Figure 17(a) shows the mean Cp profiles on the upper surface. Figure 17(b) shows the analogous curves for the internal surface, plotted using p/p_t. In Figure 17(a), the k-ε

solution with C_μ ON shows the closest agreement to minimum peak near x/D = 0, while it overpredicts the pressure near x/D=1.0, compared with the S-A and SST models. Turning the C_μ option OFF slightly improved the pressure distributions over having it ON (near x/D of 1.0). The sudden jump in pressure around x/D of 0.7, as seen in Figure 17(b), results from flow passing through the shock that contacts the nozzle wall (Figure 16(b)). For both the internal and external surfaces, the SST provides the best predicted pressure distributions.

Movements of the shock inside the nozzle yielded unsteady variations of pressure on the external surface. These variations, resulting from a shock-induced separation on the inner nozzle surface at an x/D of about 0.7, were quantified statistically using the Standard Deviation of pressure. For NPR values lower than 6, the internal surface separates, and this separation region interacting with the shock causes a low-frequency unsteady behavior on the top of the boattail surface itself, causing the pressure to oscillate. This apparent unsteadiness is related to the shockwave/boundary layer interaction and the resultant magnitude of the separation.

Figure 18 shows the instantaneous streamlines for each turbulence model that bound the separation region just inside the nozzle exit. The S-A solution with streamwise curvature correction *ON* showed the least separation off the inner surface, while the EASM model predicted the most separation. The relative positions of streamlines seen in Figure 18 is probably related to the relative magnitudes of Cp values found near x/D of 1.0 in Figure 17(a). Table 3 shows the normalized thrust and massflows for each turbulence model versus experimental data.

Table 3: Comparison of normalized massflow and thrust for various turbulence models for Subcase 2A. "cc" refers to the S-A rotation correction.

	Normalized Thrust	Normalized Massflow
Experiment	0.8063	0.9700
S-A (cc OFF)	0.7810	0.9584
S-A (cc ON)	0.7717	0.9550
SST	0.8019	0.9622
EASM	0.8587	0.9740
k-ε (C_μ OFF)	0.8456	0.9721
k-ε (C_μ ON)	0.8569	0.9714

TIME-ACCURATE CALCULATIONS

Because the variable-timestep (steady-state) solutions indicated significant variation in flow properties (failure to converge to a steady-state solution) internal and external to the nozzle, an additional time-accurate calculation using the SST model was completed for this subcase to investigate these effects. The time-accurate solution was restarted from the "steady-state" solution, and run for 458,000 iterations at a timestep of 1 nanosecond (10^{-9}). A "characteristic time" t_c for a fluid particle to move one nozzle diameter can be defined as:

$$t_c = \frac{D_{exit}}{u_{exit}}$$

where D_{exit} is the exit diameter of 0.433 ft (13.2 cm) and u_{exit} is 2,000 ft/sec (610 m/s). The total time ΔT passed over N iterations is:

$$\Delta T = N\Delta t$$

where Δt is 10^{-9} seconds. From this, one can see that at 458,000 iterations, a fluid particle has moved 2.11 nozzle diameters downstream.

Figures 19(a) and 19(b) show the mean pressure distributions external and internal to the nozzle, respectively, for the steady-state, experimental data and time-accurate solutions. These figures demonstrate that the time-averaged steady-state solutions on both surfaces are the same or nearly the same as that of the time-accurate solutions. This agreement is corroborated further by Figure 18 with plots of instantaneous streamlines, and plots of Standard Deviation of the pressure (not shown here). In Figure 19(a), the time-accurate solution predicts a slightly higher value of Cp near x/D of 0.5 compared with the steady-state solution. The time-accurate numerics appear to remove the numerical instabilities associated with the unsteady separation and enable a nearly converged solution to be obtained. The initial motivation for attempting time-accurate calculations was to obtain a more consistent set of instantaneous flowfield solutions for time-averaging of the apparent unsteady problem. However, the time-accurate calculations, with constant time stepping employed (in contrast to the local time stepping used by the steady-state solver) enabled a nearly converged solution to be obtained. Similar phenomena have been observed in calculations with separated flow on multi-element airfoil calculations at high lift[13], and in calculations of a lobed nozzle with a large separated base region[14]. While the RANS technique should be expected to provide a steady-state solution, it appears that for all of these problems with large scale flow separations, the time-accurate solver with constant time-stepping is better able to remove numerical instabilities associated with these large separated flow regions than the local time-stepping approach of the steady-state solver.

Subcase 2B: Mach 1.2, NPR 4

The results for this case resulted in a significant change in the appearance of the internal and external flowfield (in terms of Mach number contours and pressure contours) compared to Subcase 2A. The Mach number contours are shown in Figure 20, and indicate less dramatic formation of expansion and shockwaves near the exit compared to the Subcase 2A. The separated flow region on the inner nozzle wall is less than one-tenth of an inch long. Figures 21(a) and 21(b) show the pressure distributions on the external and internal surfaces, respectively. All turbulence models slightly underpredict the pressure distribution at an x/D of 0.15 as seen in Figure 21(b). The k-ε model predicts an early separation region (similar to Subcase 2A), but the EASM model predicts its location slightly better compared with Subcase 2A. The predicted pressures along the external surface (from x/D of 0.125 to 0.9) were overpredicted slightly by all turbulence models as seen in Figure 21(a). The EASM model predicts the external pressure distribution the best overall, with the SST model providing the best prediction on the internal surface (Figure 21(b)). Table 4 presents the normalized thrust and massflow for each turbulence model. Experimental thrust data was not available. The k-ε and EASM models produce the highest values of thrust of all the models.

Table 4: Comparison of normalized massflow and thrust for different turbulence models for Subcase 2B. "cc" refers to the S-A rotation correction.

	Normalized Thrust	Normalized Massflow
Experiment	N/A	0.9680
S-A (cc OFF)	0.6980	0.9526
S-A (cc ON)	0.6970	0.9527
SST	0.7009	0.9527
EASM	0.7044	0.9573
k-ε (C_μ OFF)	0.7173	0.9539
k-ε (C_μ ON)	0.7123	0.9543

CONCLUSIONS

CFD analyses of axisymmetric circular-arc boattail nozzles at transonic Mach numbers have been performed to better understand the effects of high-speed nozzle geometries on the nozzle internal flow and the surrounding boattail regions. Operation of these nozzle at lower-than-design NPRs provides a challenging flowfield for studying the capabilities of Wind's turbulence models to accurately predict nozzle aerodynamics. Boattail and internal nozzle pressure distributions computed with the Wind code have been compared with experimental data obtained in the NASA Langley 16-Foot Transonic Tunnel. Using a range of turbulence models, including the Explicit Algebraic Stress model (EASM), the experimental data pressure profiles on two nozzle geometries has been predicted reasonably well. In general, all turbulence models underpredicted the pressure distribution prior to the separated region with the EASM model providing best prediction overall, especially pressure points in the separated region at the most rearward parts of the boattail. Greater pressure differences between the jet and freestream flow appeared to improve the EASM results.

Case 2, with a convergent-divergent nozzle shape operating in overexpanded conditions, presents an even more challenging flowfield to test computational tools. The SST turbulence model best predicts the internal and external mean pressure distributions overall. The EASM model gave slightly better results on the external surface for Subcase 2B, however.

Analyzing the Wind steady-state solutions has shown that both Case 2 subcases exhibit apparent unsteadiness resulting from shock-induced separation that affects the pressure distribution on the external surface. Subsequent time-accurate analysis on the Mach 0.9, NPR 4 case using the SST model indicates that the true unsteadiness is quite less, and the numerical instabilities associated with using variable timestepping on a problem with separated regions leads to an inability to obtain a converged solution. The time-accurate solutions suggest that for problems with large scale flow separations, the time-accurate solver with constant time-stepping is better able to remove numerical instabilities associated with these large separated flow regions. The non-realistic variation in pressure seen in the steady-state calculations of Case 2 is the result of using a variable timestep in a region of the flow with large-scale separation. Constant time-stepping enabled the physically unrealistic flow oscillations to be removed. The Chien k-ε and EASM k-ε models predict the nozzle internal shock to occur upstream compared with other model predictions, resulting in a larger separation region inside the nozzle.

REFERENCES

1) Aeronautical Facilities Catalogue, ***Wind Tunnels***, NASA-RP-1132, Volume 1, National Aeronautics and Space Administration, (January 1985).

2) Abeyounis, W.K. and Putnam, L.E., ***Investigation of the Flow Field Surrounding Circular-Arc Boattail Nozzles at Subsonic Speeds***, NASA TM-1633, (May 1980).

3) Carson, G. T., Jr. and Lee, E. E., Jr., ***Experimental and Analytical Investigation of Axisymmetric Supersonic Cruise Nozzle Geometry at Mach Numbers from 0.60 to 1.30***. NASA TP-1953, (1981).

4) Nelson, C.C. and Power, G.D., ***CHSSI Project CFD-7: The NPARC Alliance Flow Simulation System***, AIAA Paper 2001-0594, (January 2001).

5) Spalart, P.R. and Allmaras, S.R., ***A One-Equation Turbulence Model for Aerodynamic Flows***, AIAA Paper 1992-0439, (January 1992).

6) Menter, F.R., ***Two-Equation Eddy Viscosity Turbulence Models for Engineering Applications***, *AIAA Journal*, Vol. 32, No. 8, pp.1598-1605, (August 1994).

7) Chien K.Y., ***Predictions of Channel and Boundary-layer Flows with a Low-Reynolds-Number Turbulence Model***, *AIAA Journal*, Vol 20, No. 1, pp.33-38.

8) Rumsey, C.L., and Gatski, T.B., and Morrison, J.H., ***Turbulence Model Predictions of Strongly Curved Flow in a U-Duct***, *AIAA Journal*, Vol. 38, No. 8., pp. 1394-1402, (2000).

9) Yoder, D. A., ***Initial Evaluation of an Algebraic Reynolds Stress Model For Compressible Turbulent Shear Flows***, AIAA Paper 2003-0548, (January 2003).

10) Sarkar, S., Erlebacher, G., and Kreiss, H.O., ***The Analysis and Modeling of Dilatational Terms in Compressible Turbulence***, *Journal of Fluid Mechanics*, Vol. 227, pp. 473-493, (1991).

11) Rodi, W., ***A New Algebraic Relation for Calculating the Reynolds Stresses***, Z. Ang. Math. Mech., Vol. 56, pp. T219-T221, (1976).

12) *GRIDGEN Version 15*, ***User Manual***, Pointwise, Inc., Bedford, Texas, (1998).

13) Ying, S. X., Spaid, F.W., McGinley, C.B., and Rumsey, C.L., ***Investigation of Confluent Boundary Layers in High-Lift Flows***, *Journal of Aircraft*, Vol. 36, No. 3, pp. 550-562, (May-June 1999).

14) Georgiadis, N.J., Rumsey, C.L., Yoder, D.A., and Zaman, K.B.M.Q., ***Effects of RANS Turbulence Modeling on Calculations of Lobed Nozzle Flowfields***, AIAA Paper 2003-1271, (January 2003).

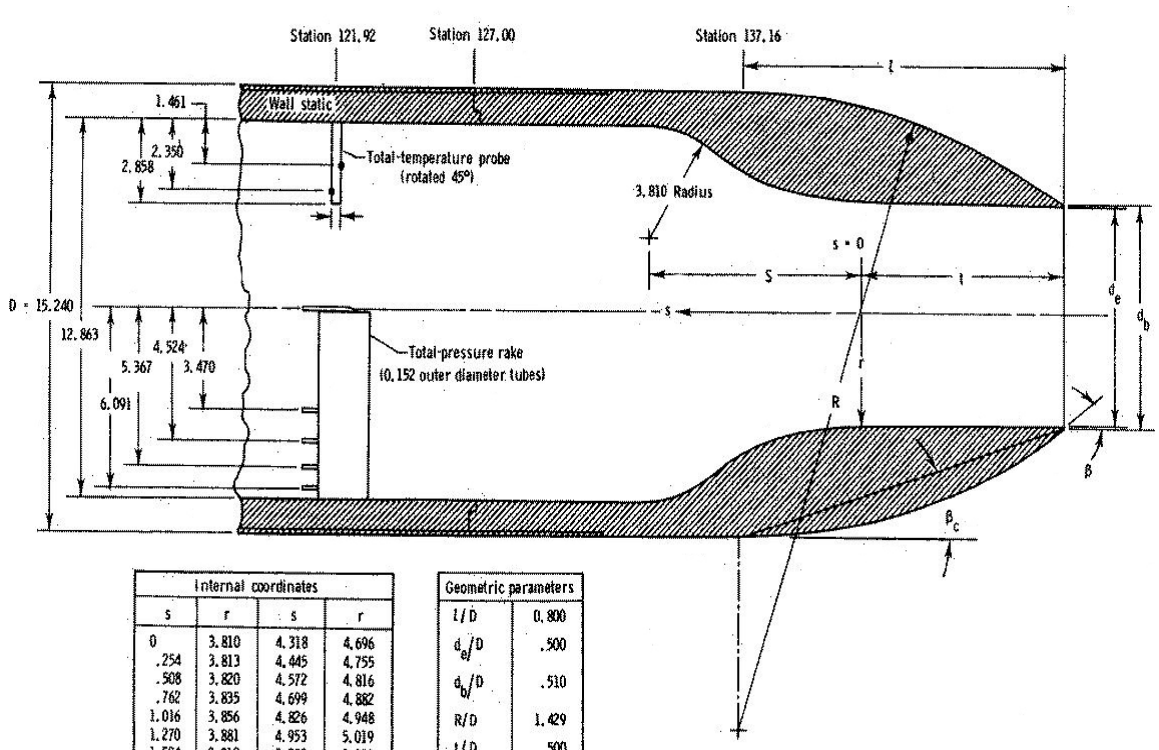

Internal coordinates			
s	r	s	r
0	3.810	4.318	4.696
.254	3.813	4.445	4.755
.508	3.820	4.572	4.816
.762	3.835	4.699	4.882
1.016	3.856	4.826	4.948
1.270	3.881	4.953	5.019
1.524	3.912	5.080	5.090
1.778	3.950	5.207	5.169
2.032	3.993	5.334	5.248
2.286	4.041	5.461	5.334
2.540	4.097	5.588	5.420
2.794	4.161	5.715	5.514
3.048	4.229	5.842	5.611
3.302	4.308	5.969	5.715
3.555	4.392	6.096	5.822
3.810	4.483	6.223	5.939
3.937	4.534	6.350	6.060
4.064	4.585	6.477	6.190
4.191	4.641		

Geometric parameters	
l/D	0.800
d_e/D	.500
d_b/D	.510
R/D	1.429
t/D	.500
S/D	.533
β, deg	34.054
β_c, deg	17.027

Figure 1: Schematic of nozzle geometry (units in cm) investigated in Case 1.

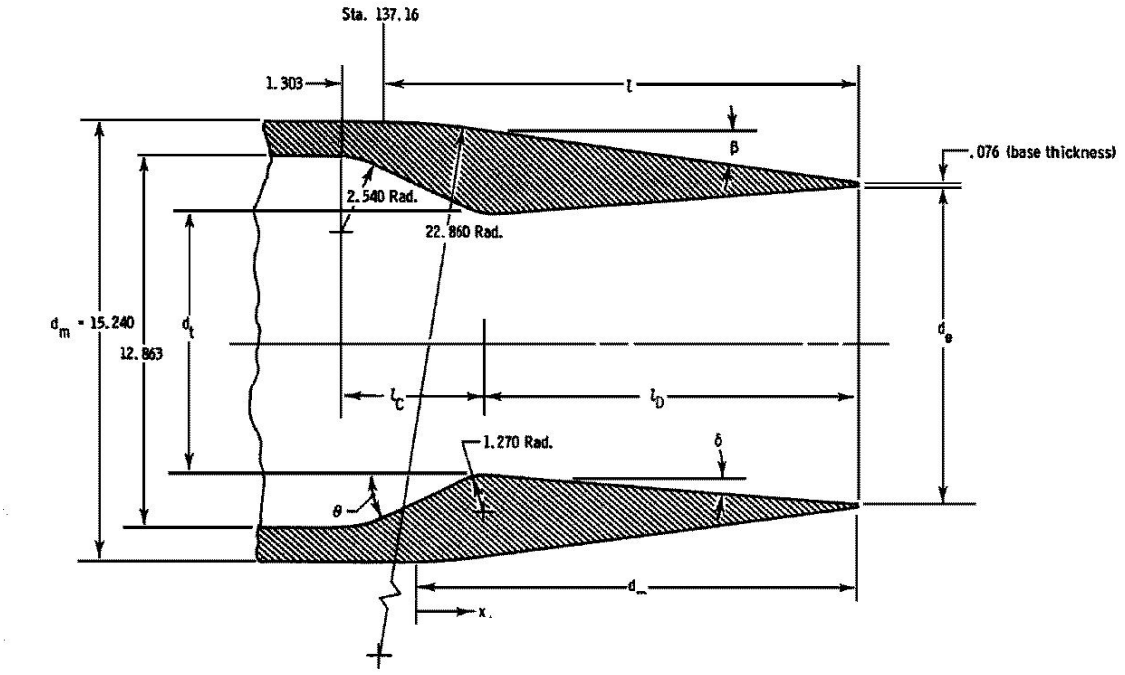

Figure 2: Schematic of nozzle geometry (units in cm) investigated in Case 2.

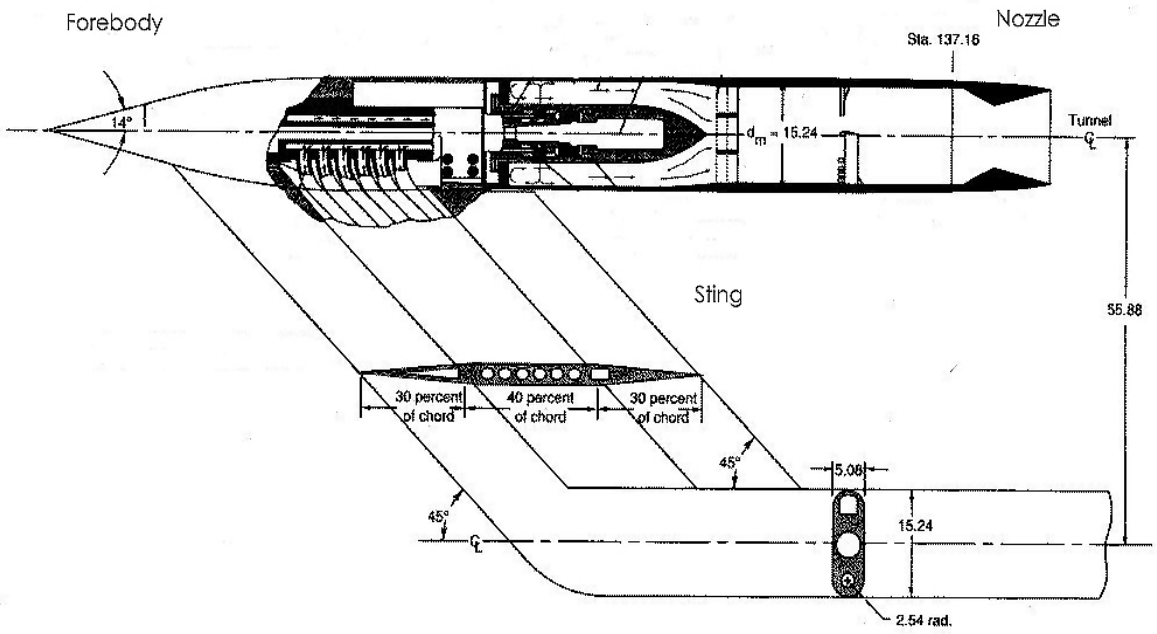

Figure 3: Schematic of NASA Langley experimental rig (forebody/nozzle/support).

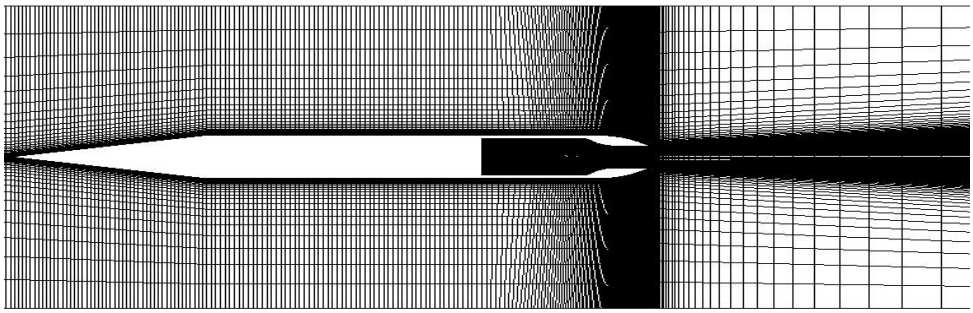

Figure 4(a): Computational grid for Case 1 showing the forebody and nozzle structure.

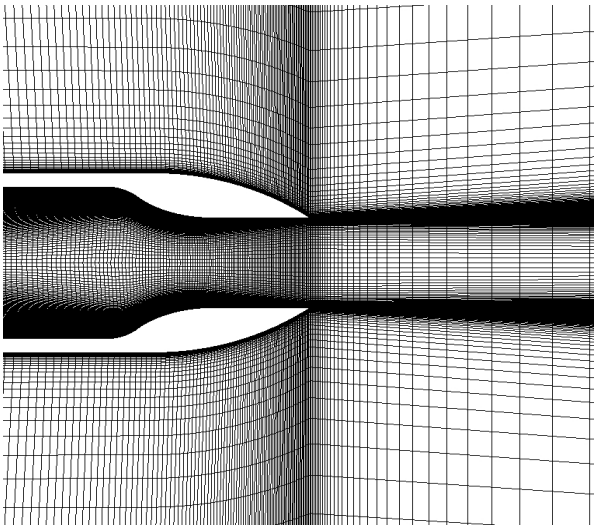

Figure 4(b): Close-up view of Case 1 grid near the nozzle exit.

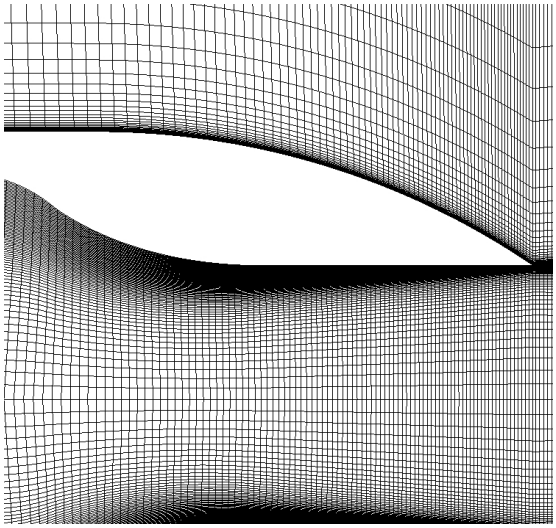

Figure 4(c): Close-up view of Case 1 grid highlighting the nozzle afterbody.

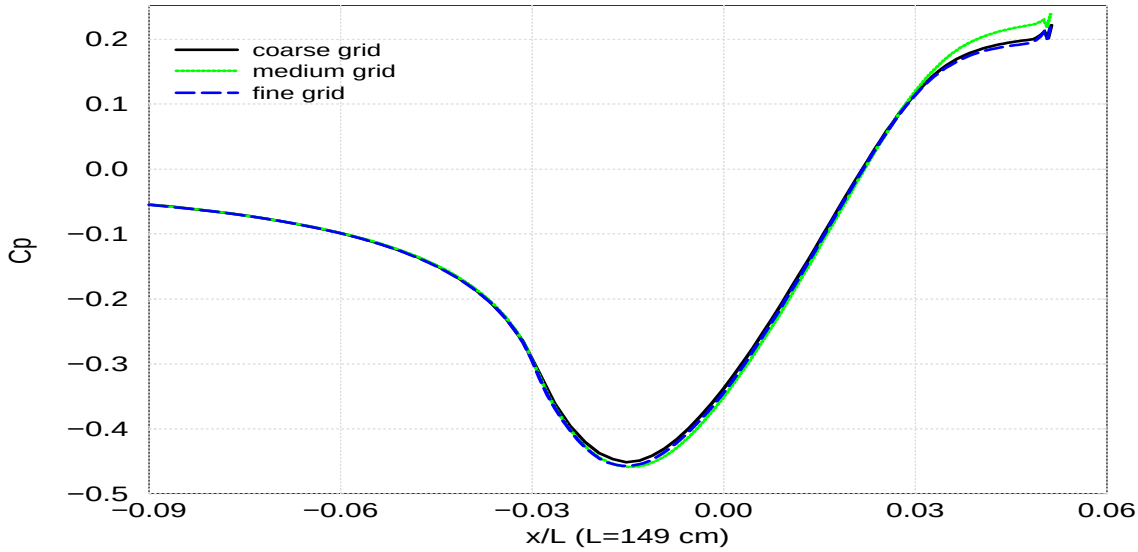

Figure 5: Grid dependence plot of Cp values on the upper boattail surface for coarse, medium and fine grids for Case 1.

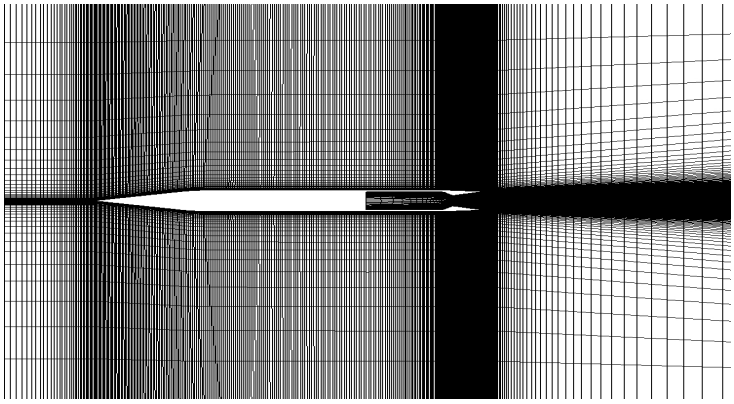

Figure 6(a): Computational grid for Case 2 showing the fore-body and nozzle structure.

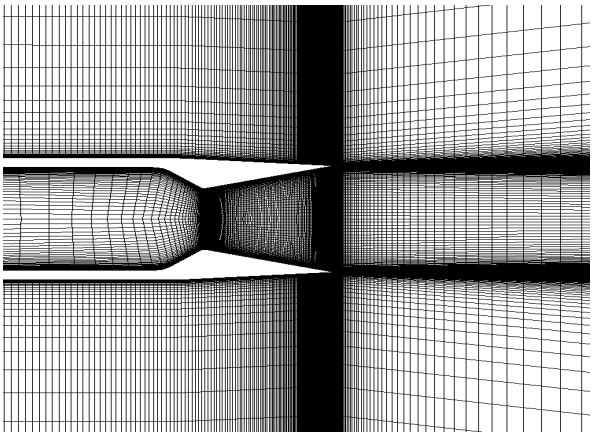

Figure 6(b): Close-up view of Case 2 grid near the nozzle exit.

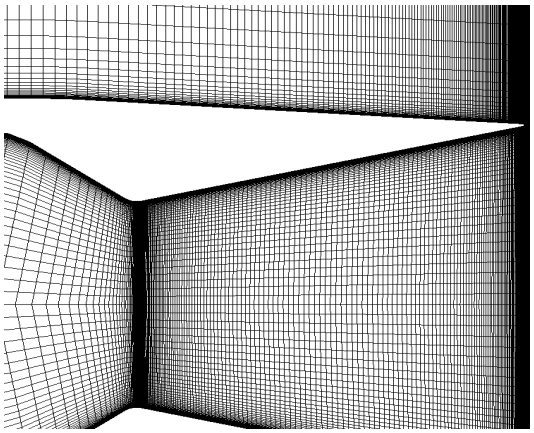

Figure 6(c): Close-up view of Case 2 grid highlighting the nozzle afterbody.

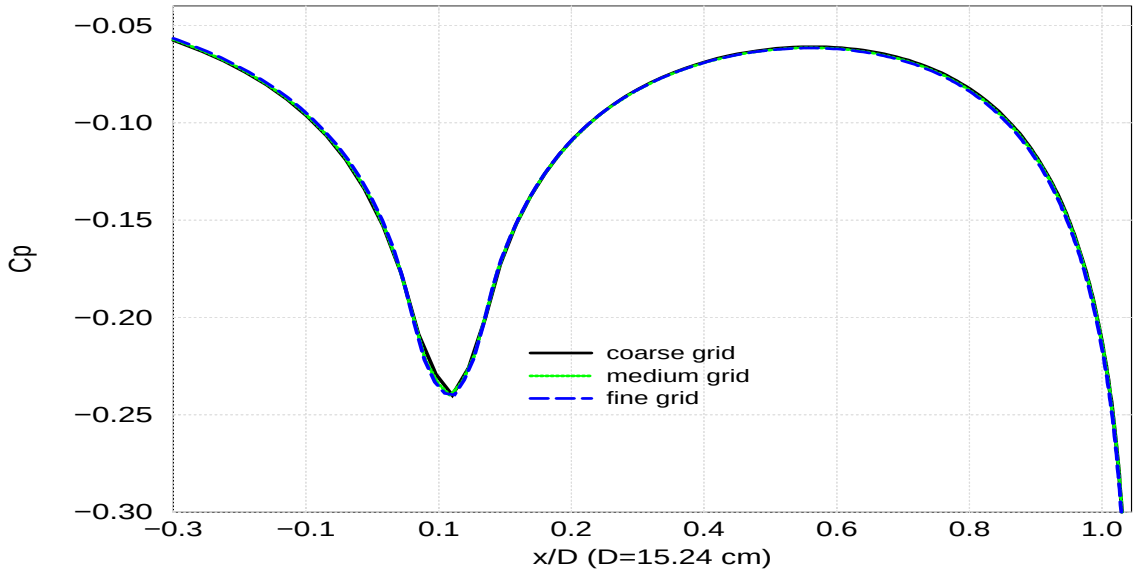

Figure 7: Grid dependence plot of mean Cp values on the upper boattail surface for coarse, medium and fine grids for Case 2.

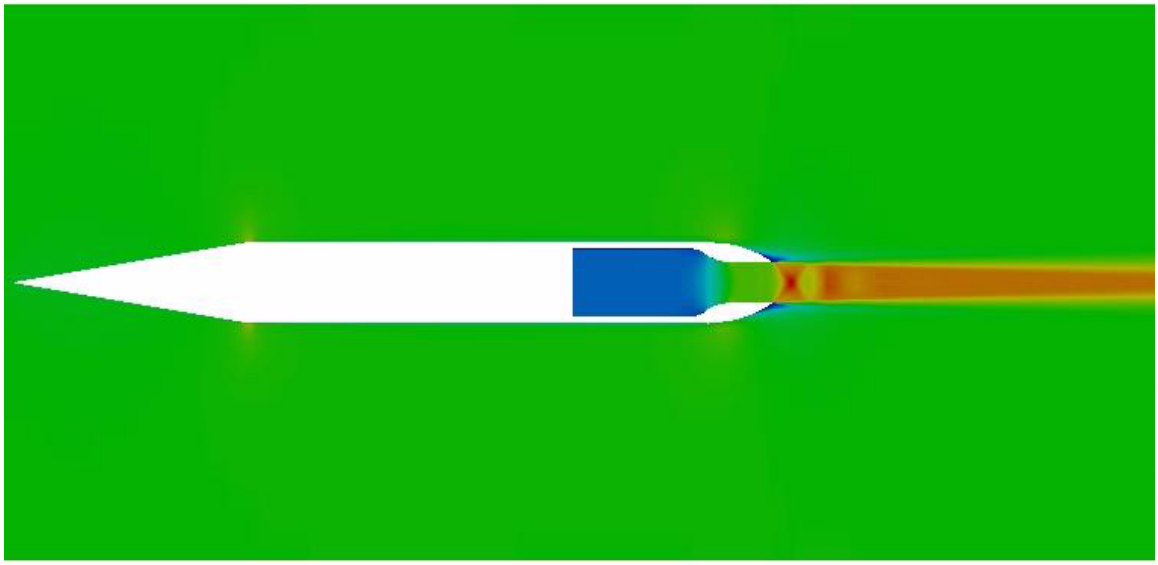

Figure 8(a): Mach number contours for Subcase 1A.

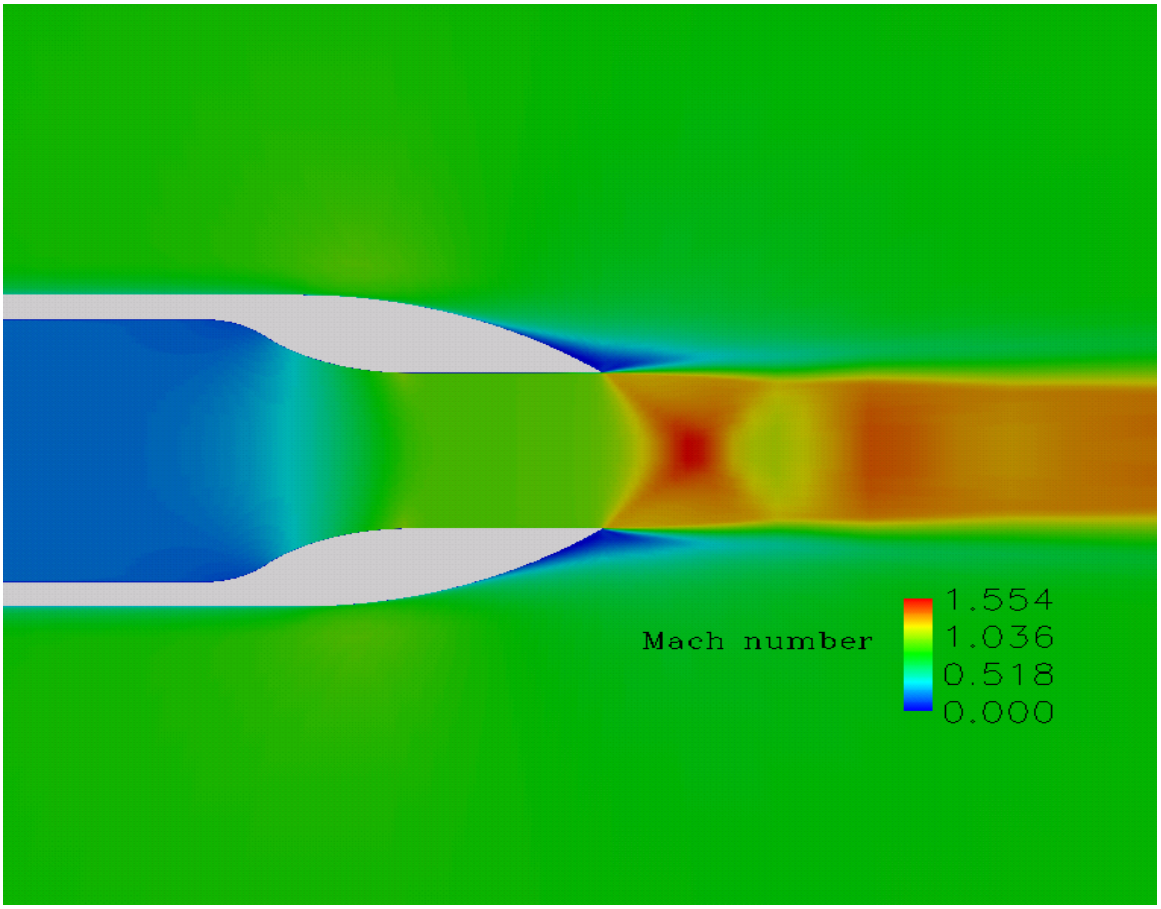

Figure 8(b): Mach number contours at for Subcase 1A (closeup view).

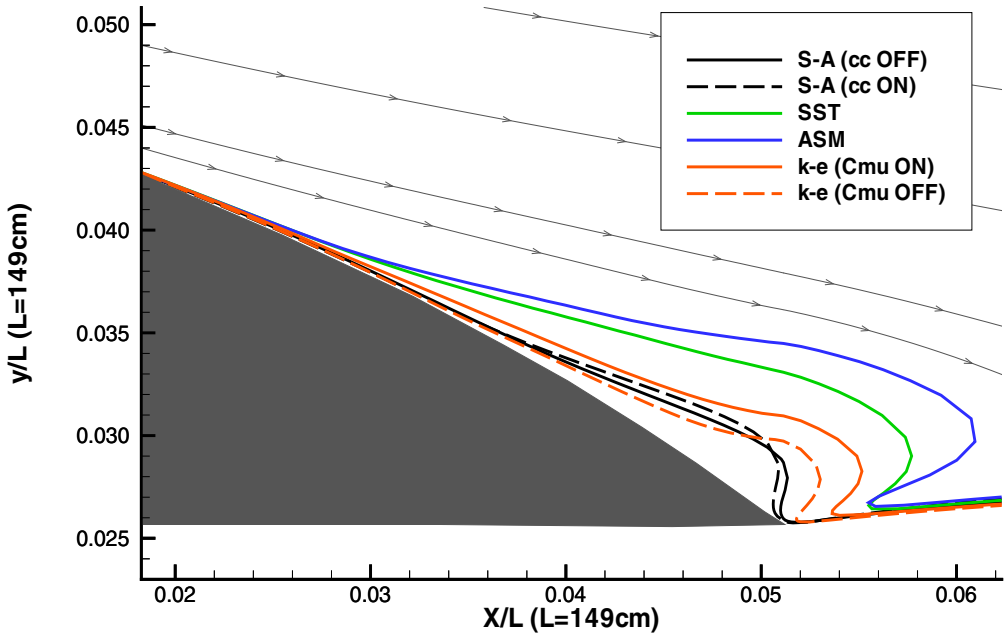

Figure 9: Streamlines defining the separation relative separation region on the external surface for Subcase 1A. The shaded region indicates the nozzle structure near the exit. The gray lines are reference streamlines.

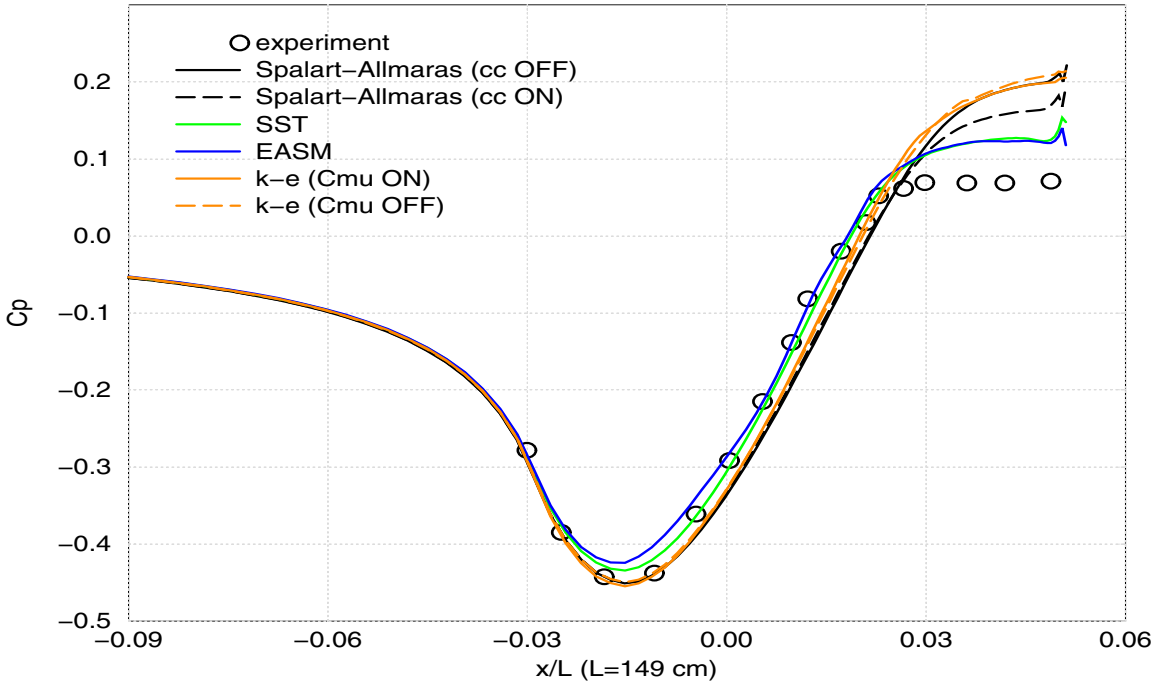

Figure 10: Cp profiles on the upper surface for Subcase 1A.

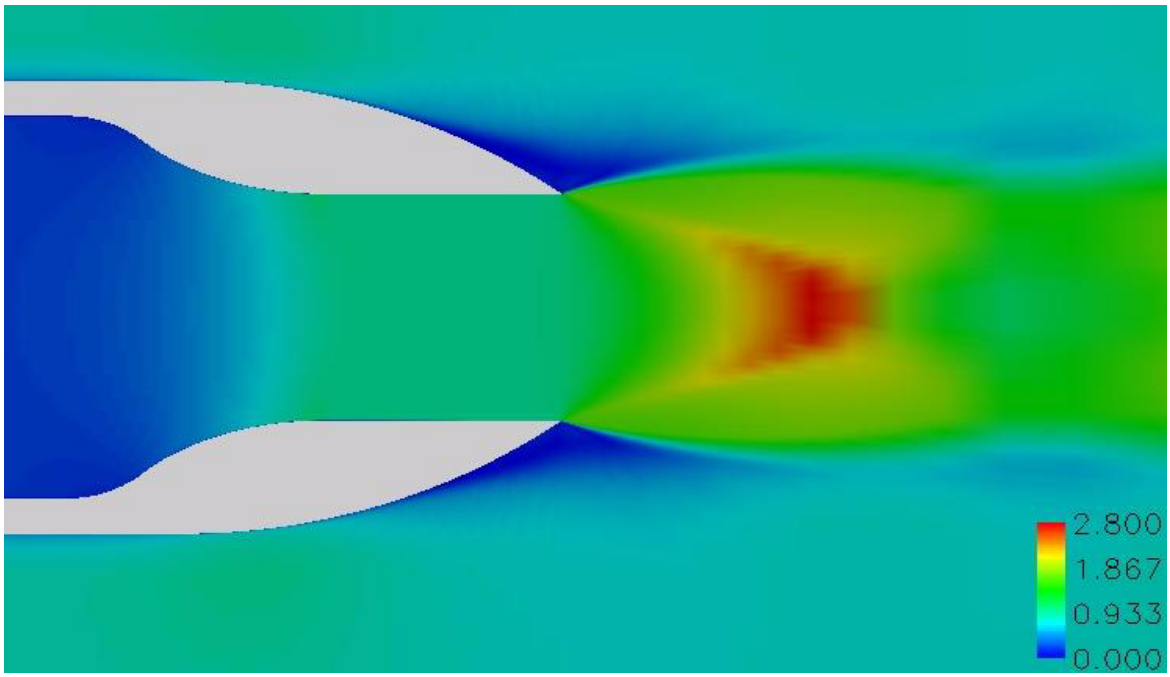

Figure 11: Mach number contours for Subcase 1B (closeup view).

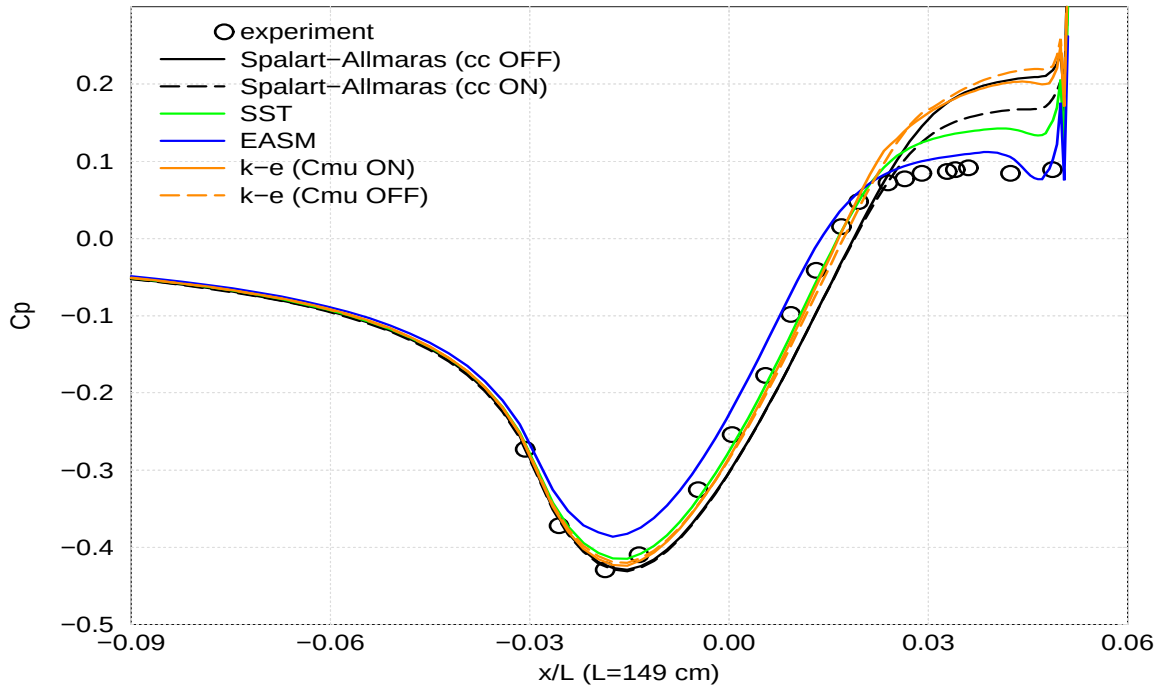

Figure 12: Cp profiles on the upper surface for Subcase 1B.

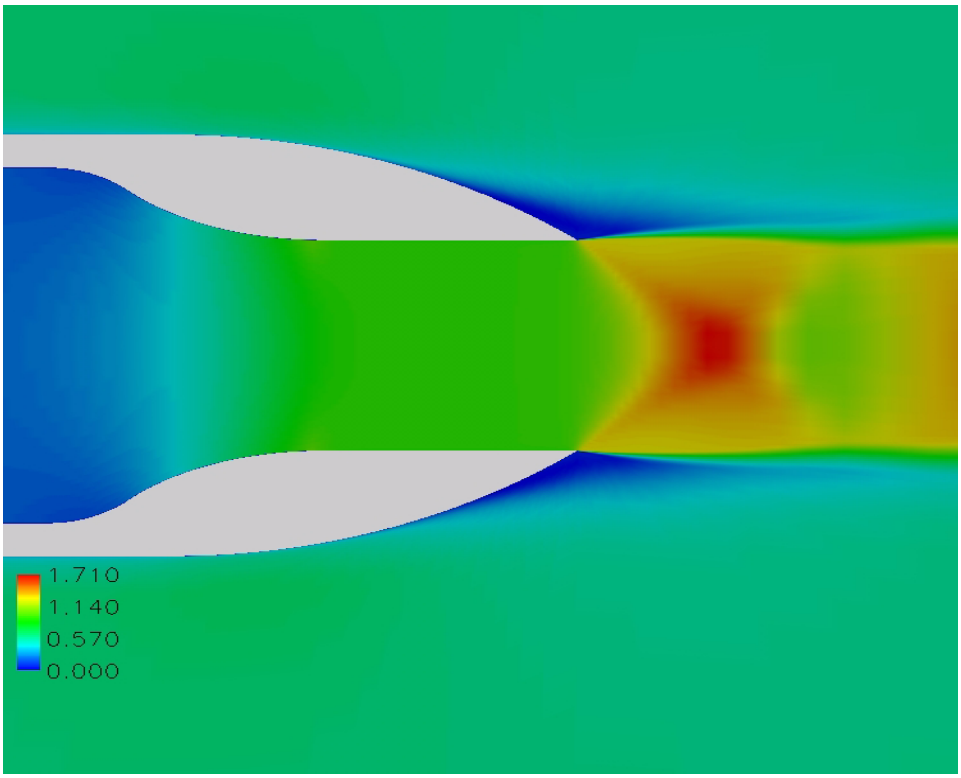

Figure 13: Mach number contours for Subcase 1C (closeup view).

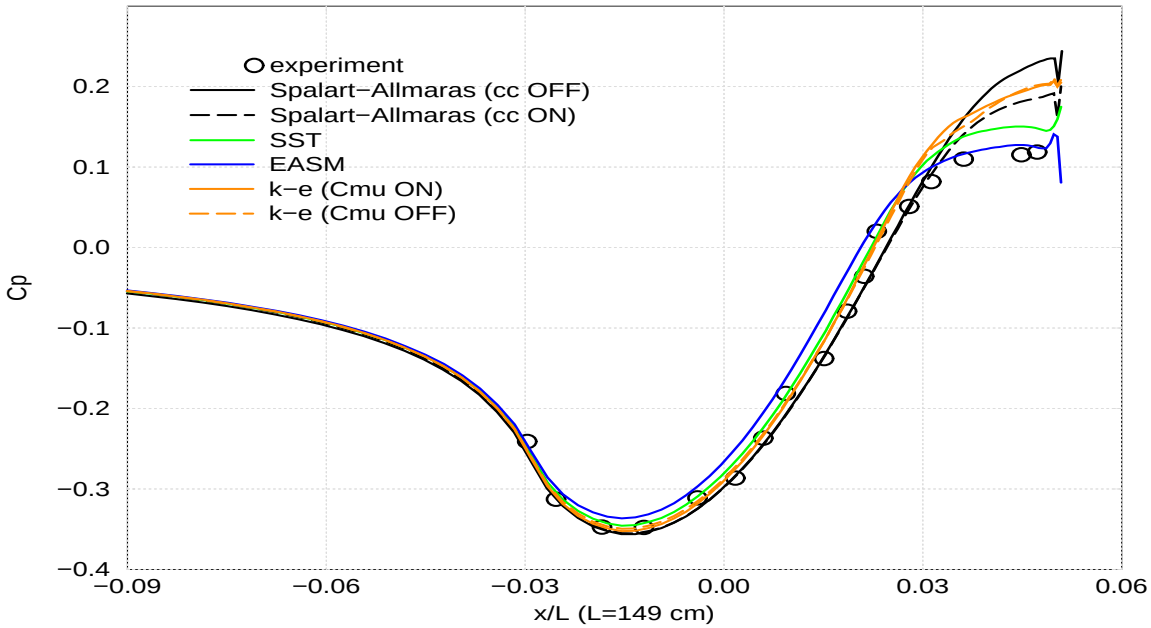

Figure 14: Cp profiles on the upper surface for Subcase 1C.

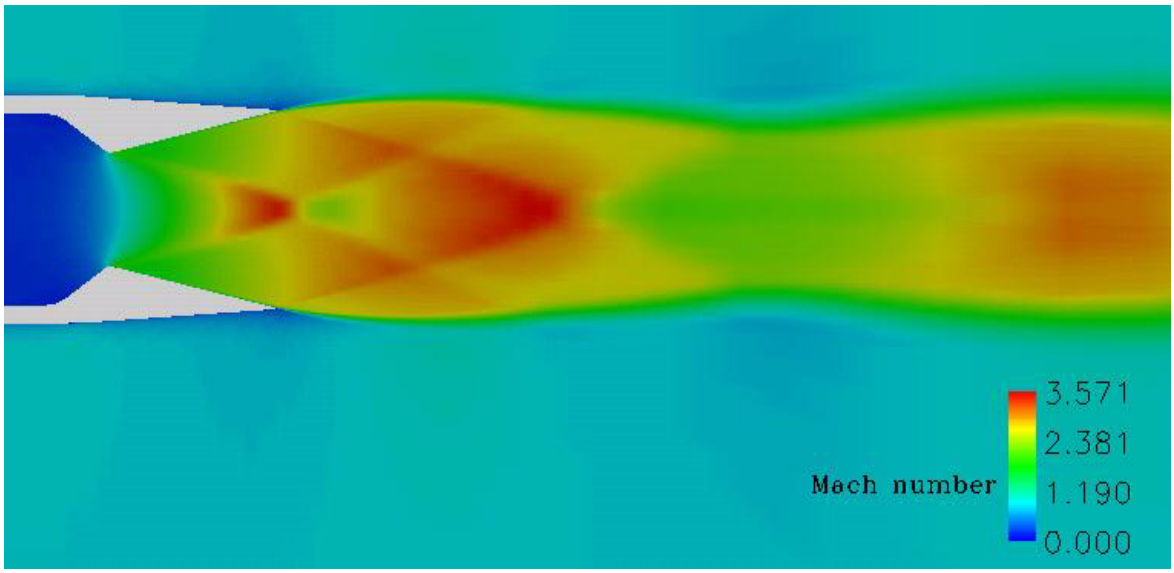

Figure 15: Mach number contours using the Spalart-Allmaras model at the design NPR of 21.23 and Mach number 0.9.

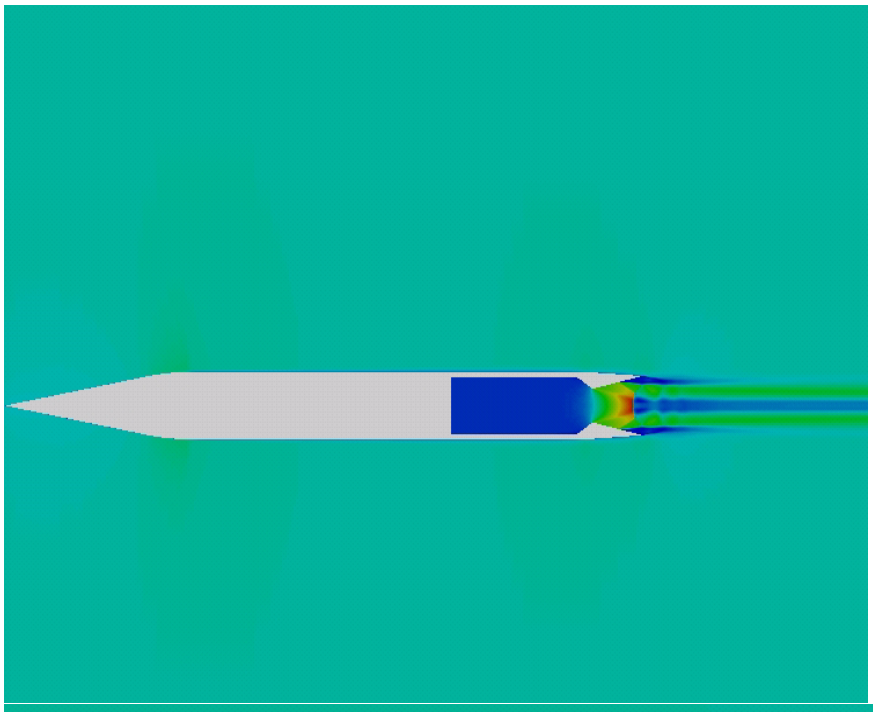

Figure 16(a): Mach number contours for Subcase 2A highlighting forebody geometry.

Figure 16(b): Closeup of nozzle.

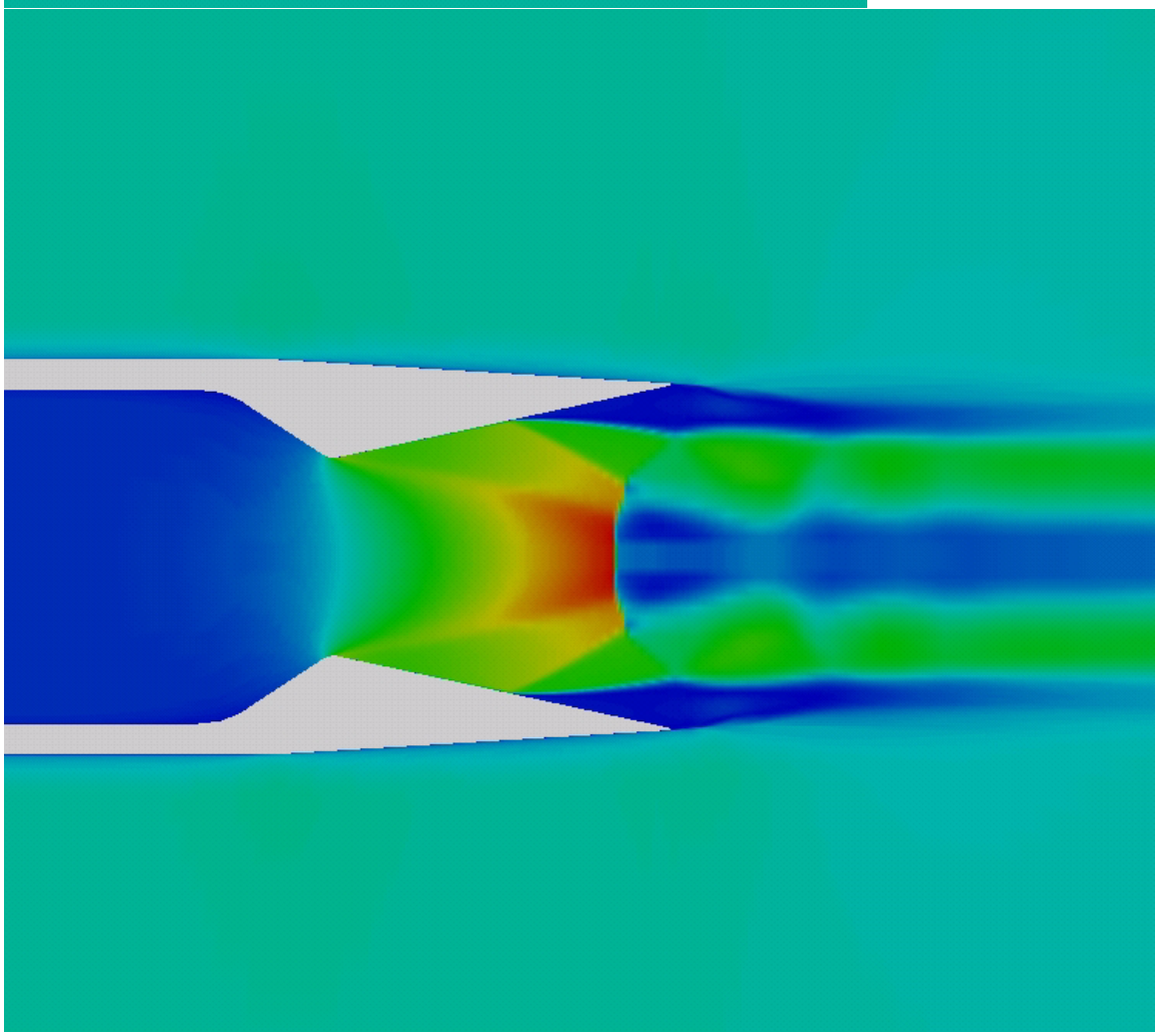

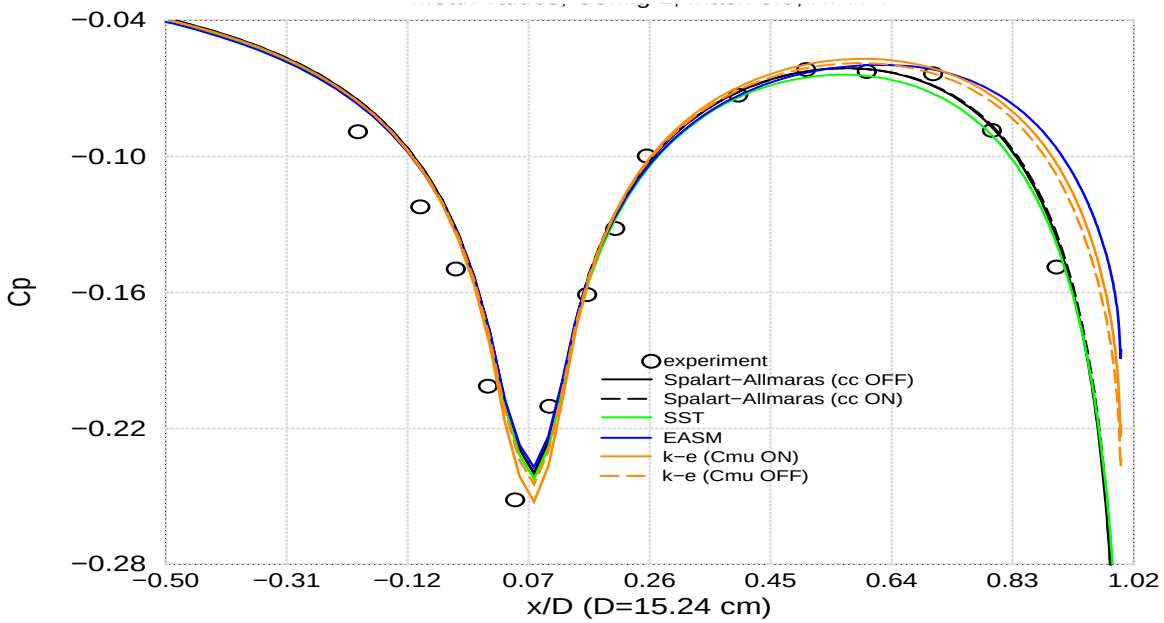

Figure 17(a): Mean Cp profiles on the upper boattail surface for Subcase 2A.

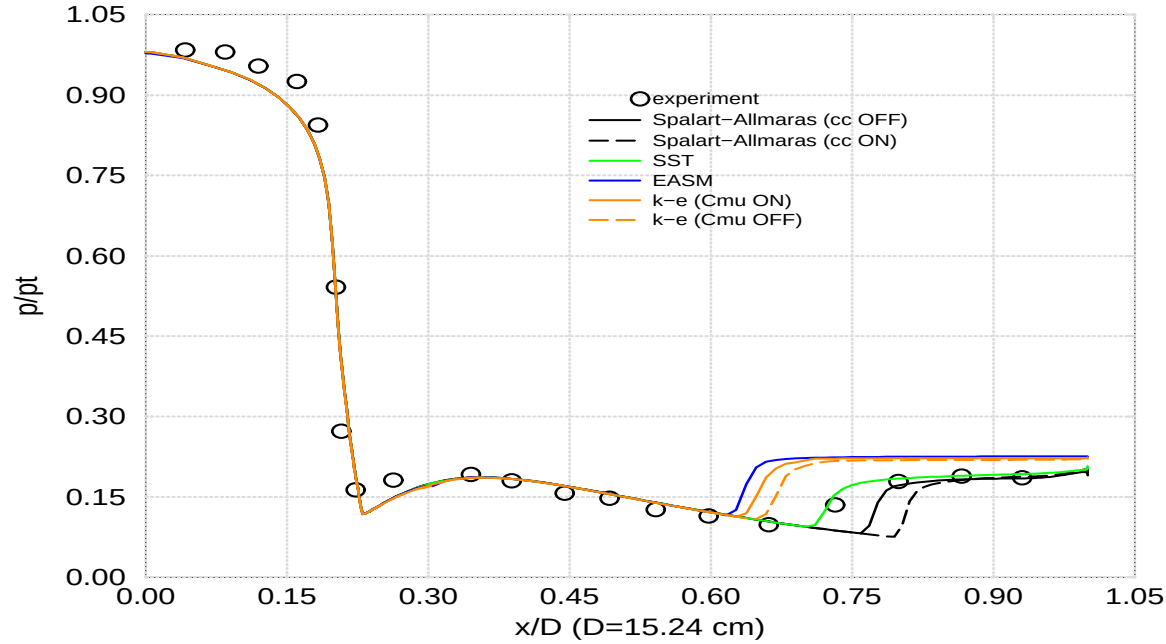

Figure 17(b): Instantaneous normalized pressure profiles on the bottom (inner) nozzle surface for Subcase 2A.

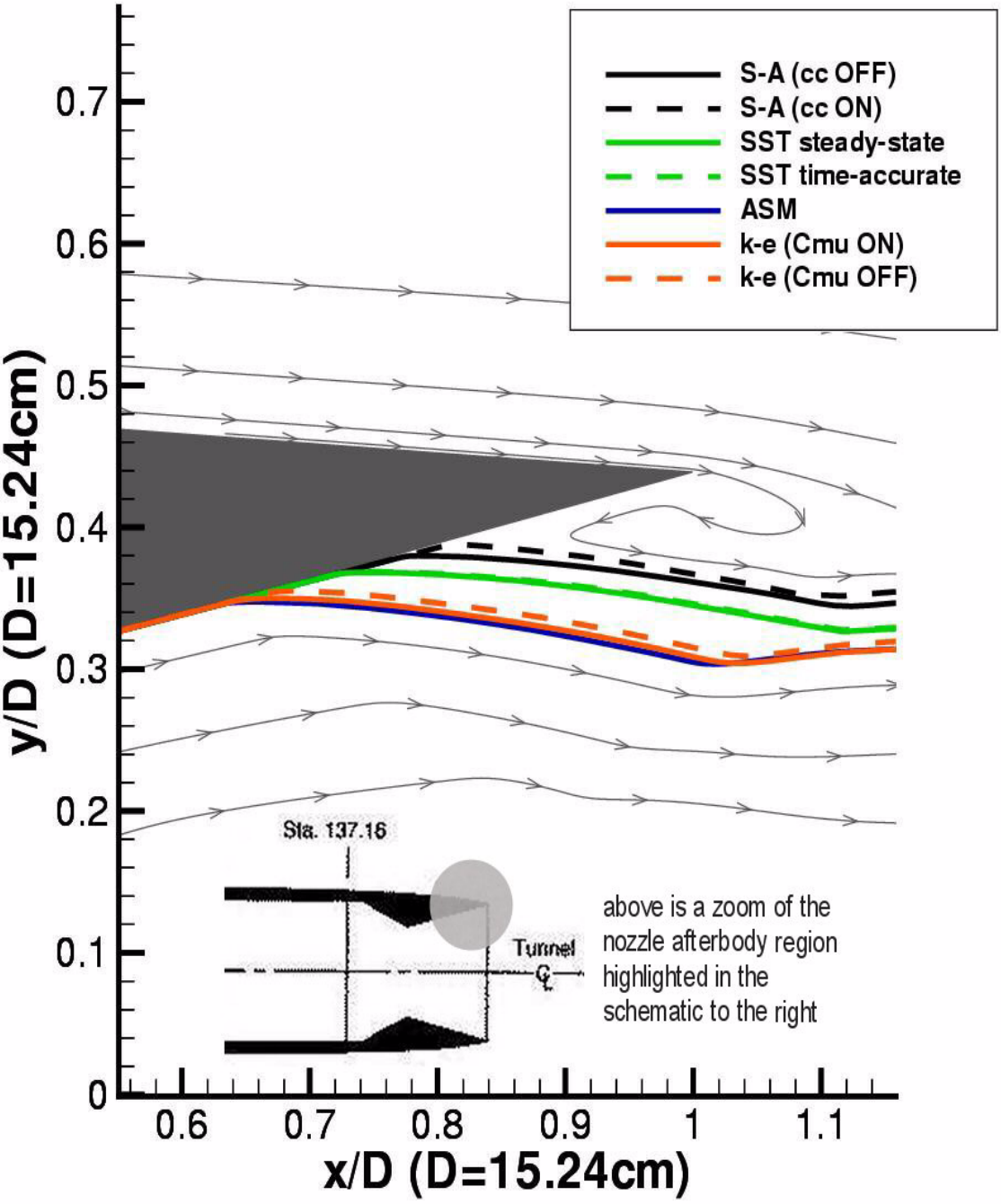

Figure 18: Streamlines defining the separation relative separation region for Subcase 2A. Streamlines start at the 7th gridpoint off the wall in the nozzle throat. The shaded region indicates the nozzle afterbody structure. The gray streamlines are reference streamlines.

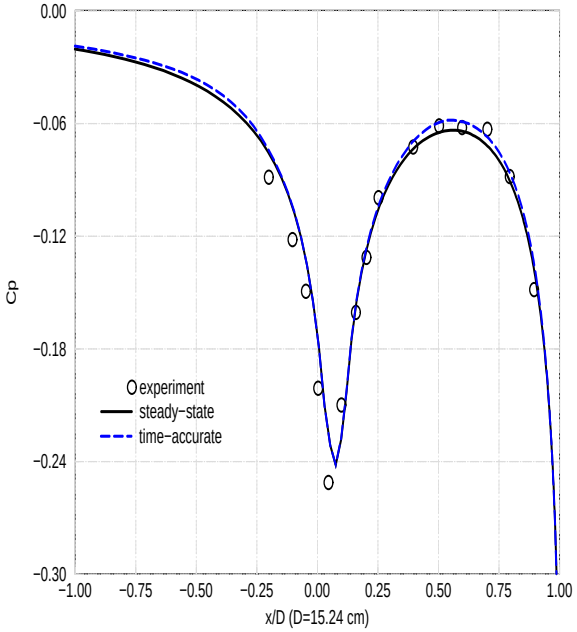

Figure 19(a): Cp curves on external surface for Subcase 2A with the SST model.

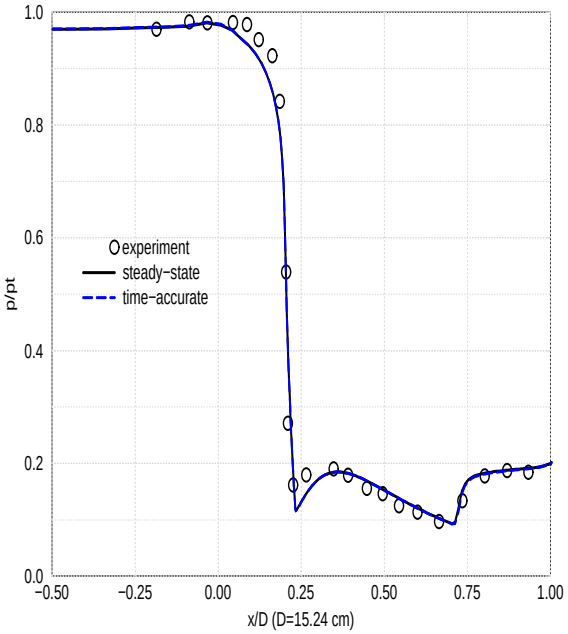

Figure 19(b): Normalized pressure (p/p_t) curves on internal surface for Subcase 2A with the SST model.

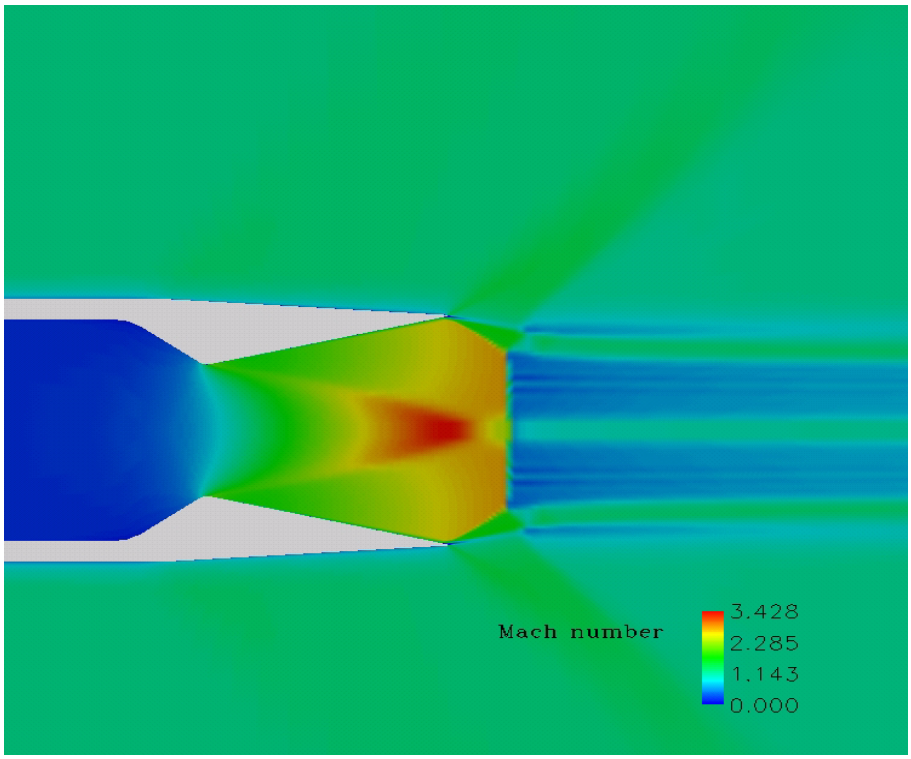

Figure 20: Mach number contours for Subcase 2B with the Spalart-Allmaras model.

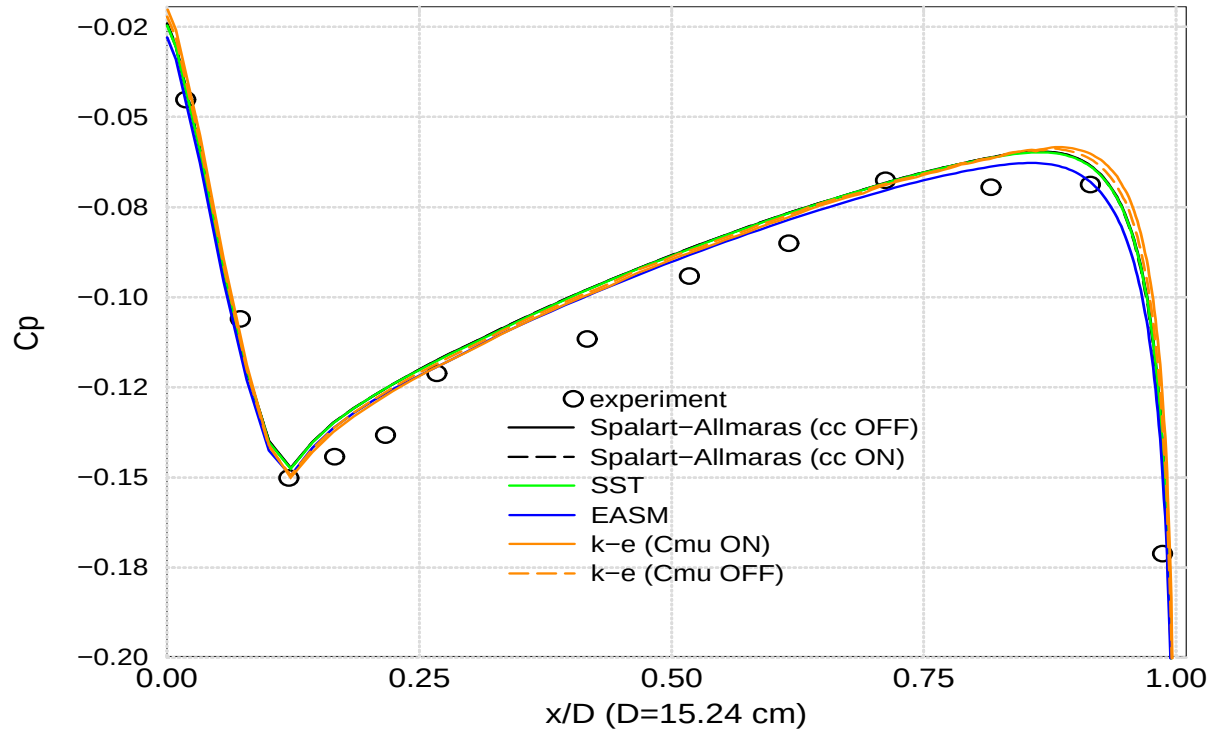

Figure 21(a): Mean Cp profiles on the upper boattail surface for Subcase 2B.

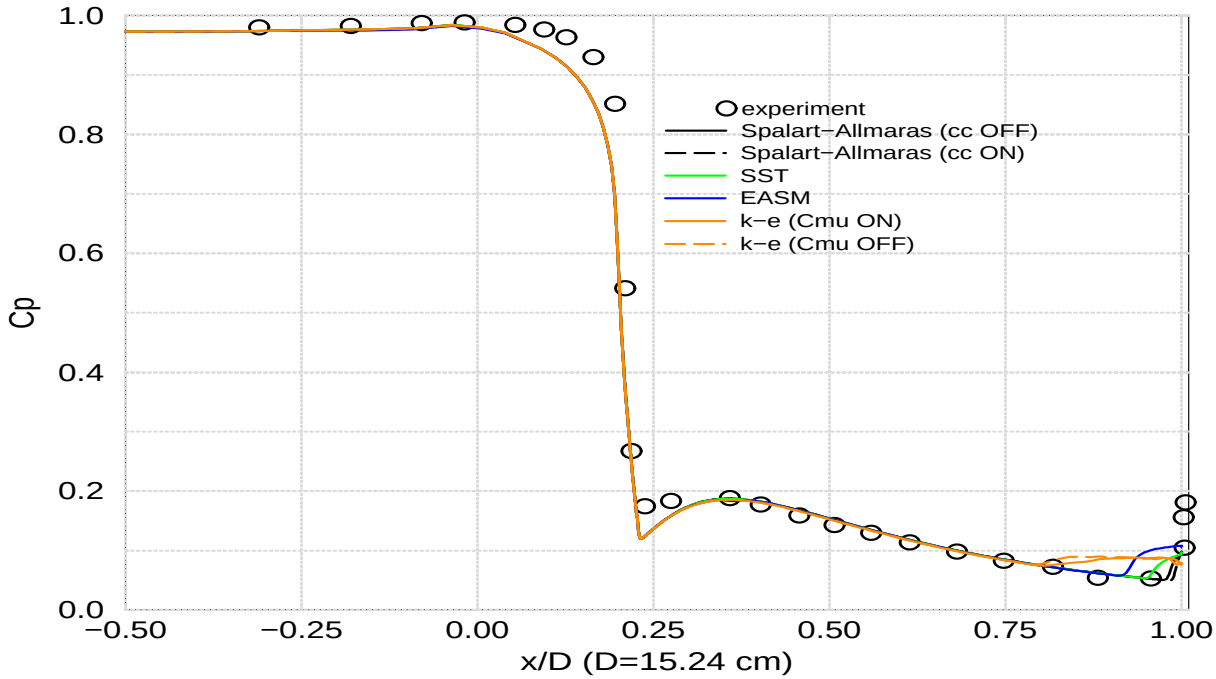

Figure 21(b): Mean p/p_t profiles on the internal nozzle surface for Subcase 2B.

REPORT DOCUMENTATION PAGE

Form Approved
OMB No. 0704-0188

1. AGENCY USE ONLY (*Leave blank*)	2. REPORT DATE	3. REPORT TYPE AND DATES COVERED
	November 2003	Technical Memorandum

4. TITLE AND SUBTITLE

Computations of Internal and External Axisymmetric Nozzle Aerodynamics at Transonic Speeds

5. FUNDING NUMBERS

WBS–22–708–73–22

6. AUTHOR(S)

Teryn DalBello, Nicholas Georgiadis, Dennis Yoder, and Theo Keith

7. PERFORMING ORGANIZATION NAME(S) AND ADDRESS(ES)

National Aeronautics and Space Administration
John H. Glenn Research Center at Lewis Field
Cleveland, Ohio 44135–3191

8. PERFORMING ORGANIZATION REPORT NUMBER

E–14256

9. SPONSORING/MONITORING AGENCY NAME(S) AND ADDRESS(ES)

National Aeronautics and Space Administration
Washington, DC 20546–0001

10. SPONSORING/MONITORING AGENCY REPORT NUMBER

NASA TM—2003-212731

11. SUPPLEMENTARY NOTES

Prepared for the 39th Combustion/27th Airbreathing Propulsion/21st Propulsion Systems Hazards/Third Modeling and Simulation Joint Subcommittee Meeting sponsored by the Joint-Army-Navy-Air Force Interagency Propulsion Committee (JANNAF), Colorado Springs, Colorado, December 1–5, 2003. Teryn DalBello and Theo Keith, University of Toledo, Toledo, Ohio 43606; and Nicholas Georgiadis and Dennis Yoder, NASA Glenn Research Center. Responsible person, Teryn DalBello, organization code 5860, 216–433–8412.

12a. DISTRIBUTION/AVAILABILITY STATEMENT

Unclassified - Unlimited
Subject Categories: 02 and 34 Distribution: Nonstandard

Available electronically at http://gltrs.grc.nasa.gov

This publication is available from the NASA Center for AeroSpace Information, 301–621–0390.

12b. DISTRIBUTION CODE

13. ABSTRACT ***(Maximum 200 words)***

Computational Fluid Dynamics (CFD) analyses of axisymmetric circular-arc boattail nozzles have been completed in support of NASA's Next Generation Launch Technology Program to investigate the effects of high-speed nozzle geometries on the nozzle internal flow and the surrounding boattail regions. These computations span the very difficult transonic flight regime, with shock-induced separations and strong adverse pressure gradients. External afterbody and internal nozzle pressure distributions computed with the Wind code are compared with experimental data. A range of turbulence models were examined in Wind, including an Explicit Algebraic Stress model (EASM). Computations on two nozzle geometries have been completed at freestream Mach numbers ranging from 0.6 to 0.9, driven by nozzle pressure ratios (NPR) ranging from 2.9 to 5. Results obtained on converging-only geometry indicate reasonable agreement to experimental data, with the EASM and Shear Stress Transport (SST) turbulence models providing the best agreement. Calculations completed on a converging-diverging geometry involving large-scale internal flow separation did not converge to a true steady-state solution when run with variable timestepping (steady-state). Calculations obtained using constant timestepping (time-accurate) indicate less variations in flow properties compared with steady-state solutions. This failure to converge to a steady-state solution was found to be the result of difficulties in using variable time-stepping with large-scale separations present in the flow. Nevertheless, time-averaged boattail surface pressure coefficient and internal nozzle pressures show fairly good agreement with experimental data. The SST turbulence model demonstrates the best over-all agreement with experimental data.

14. SUBJECT TERMS

Transonic; Separation; Boattail; Nozzle; Turbulence; Convergent-divergent; Wind; Axisymmetric; Afterbody

15. NUMBER OF PAGES

28

16. PRICE CODE

17. SECURITY CLASSIFICATION OF REPORT	18. SECURITY CLASSIFICATION OF THIS PAGE	19. SECURITY CLASSIFICATION OF ABSTRACT	20. LIMITATION OF ABSTRACT
Unclassified	Unclassified	Unclassified	